Received: 23 August 2023 | Revised: 10 February 2024 | Accepted: 10 March 2024

DOI: 10.1111/joa.14041

Journal of Anatomy ANATOMICAL SOCIETY WILEY

ORIGINAL ARTICLE

Estimation of the forces exerted on the limb long bones of a white rhinoceros (*Ceratotherium simum*) using musculoskeletal modelling and simulation

Cyril Etienne[1] | **Alexandra Houssaye**[1] | **Michael J. Fagan**[2] | **John R. Hutchinson**[3]

[1]UMR 7179 Mécanismes adaptatifs et Évolution (MECADEV), Centre National de la Recherche Scientifique, Muséum National d'Histoire Naturelle, Paris, France

[2]Department of Engineering, Medical and Biological Engineering Research Group, University of Hull, Hull, UK

[3]Structure and Motion Laboratory, Royal Veterinary College, Hatfield, UK

Correspondence

Cyril Etienne, UMR 7179 Mécanismes adaptatifs et Évolution (MECADEV), Centre National de la Recherche Scientifique, Muséum National d'Histoire Naturelle, Paris, France.
Email: cyril.etienne@cri-paris.org

Funding information

H2020 European Research Council, Grant/Award Number: ERC-2016-STG-715300; Learning Planet Institute/ Université Paris Cité

Abstract

Heavy animals incur large forces on their limb bones, due to the transmission of body weight and ground reaction forces, and the contractions of the various muscles of the limbs. This is particularly true for rhinoceroses, the heaviest extant animals capable of galloping. Several studies have examined their musculoskeletal system and the forces their bones incur, but no detailed quantification has ever been attempted. Such quantification could help understand better the link between form and function in giant land animals. Here we constructed three-dimensional musculoskeletal models of the forelimb and hindlimb of *Ceratotherium simum*, the heaviest extant rhino species, and used static optimisation (inverse) simulations to estimate the forces applied on the bones when standing at rest, including magnitudes and directions. Overall, unsurprisingly, the most active muscles were antigravity muscles, which generate moments opposing body weight (thereby incurring the ground reaction force), and thus keep the joints extended, avoiding joint collapse via flexion. Some muscles have an antigravity action around several joints, and thus were found to be highly active, likely specialised in body weight support (*ulnaris lateralis*; digital flexors). The humerus was subjected to the greatest amount of forces in terms of total magnitude; forces on the humerus furthermore came from a great variety of directions. The radius was mainly subject to high-magnitude compressive joint reaction forces, but to little muscular tension, whereas the opposite pattern was observed for the ulna. The femur had a pattern similar to that of the humerus, and the tibia's pattern was intermediate, being subject to great compression in its caudal side but to great tension in its cranial side (i.e. bending). The fibula was subject to by far the lowest force magnitude. Overall, the forces estimated were consistent with the documented morphofunctional adaptations of *C. simum's* long bones, which have larger insertion areas for several muscles and a greater robusticity overall than those of lighter rhinos, likely reflecting the intense forces we estimated here. Our estimates of muscle and bone (joint) loading regimes for this giant tetrapod improve the understanding of the

---

links between form and function in supportive tissues and could be extended to other aspects of bone morphology, such as microanatomy.

KEYWORDS
biomechanics, joints, locomotion, long bones, musculoskeletal system, OpenSim, rhinoceros

1 | INTRODUCTION

Large land vertebrates (i.e. above 1000 kg body mass) need strong muscles to stand and move, delivering intense forces to their limb bones, which are also subject to reaction forces at the articulations (Biewener, 1989; Biewener & Patek, 2018; Hildebrand et al., 1985; Hutchinson, 2021). This is particularly true for rhinoceroses, especially white rhinoceroses (*Ceratotherium simum*), as they are the fourth heaviest species of land mammals on Earth today, with adult masses of 1350–3500 kg (average 2300 kg; Dinerstein, 2011); only smaller than the three species of elephants. *C. simum* is the heaviest mammal that is still capable of adopting a galloping gait, a 'four-beat' asymmetrical footfall pattern in which all four limbs are off the ground at one point of the locomotion cycle (Alexander & Pond, 1992; Garland, 1983; Hildebrand, 1980, 1989). Moreover, their limb joints appear more flexed than in elephants, suggesting that relatively greater muscular forces should be necessary to keep the joints extended, due to the greater moment arms of body weight and the ground reaction force (Biewener & Patek, 2018). The functional morphology of their limb long bones has been studied in some detail, and their musculature has recently been described, with quantification of maximal possible force outputs (Etienne et al., 2021; Mallet et al., 2019, 2020). The pressures on the feet of rhinoceroses during walking have been measured and compared with the incidence of pathologies (Dudley et al., 2014; Panagiotopoulou et al., 2019; Regnault et al., 2013). However, the precise partitioning, activation levels and directions of those muscular forces in normal loading conditions (as opposed to the maximal forces possibly exerted by muscles) are difficult to quantify. A better characterisation of muscular forces, along with joint reaction forces, is essential to more precisely estimate the links between forces experienced and bone shape and microanatomy in large animals such as rhinos (see Alexander & Pond, 1992; Houssaye et al., 2016) and should clarify linkages between form and function in the musculoskeletal system of large animals.

The forces exerted by limb muscles, their directions and the magnitudes and directions of the joint reaction forces they incur are controlled, in a complex pattern, by the nervous system (Biewener & Patek, 2018). Muscles seldom contract at their maximum isometric forces but rather adjust their contractions to simply keep the animal standing or to generate movements. Maximal activation is only expected during extreme high-speed locomotion (such as galloping) or other intense athletic performance, which seems to be infrequent in rhinos. African rhinos spend 50%–60% of a 24-h cycle foraging, thus standing still or walking slowly, surely involving smaller forces. The rest of their time is spent resting or wallowing (Dinerstein, 2011). Measuring internal forces in vivo is challenging and typically invasive and thus practically impossible for rhinoceroses. Instead, it is possible to estimate muscular and joint reaction forces via biomechanical computer modelling and simulation (e.g. Demuth et al., 2023; Seth et al., 2018). In humans, such models are often used to study the basic science of locomotor dynamics as well as more clinical applications (Park et al., 2019; Rajagopal et al., 2016; Seth et al., 2018; van der Krogt et al., 2016; Willson et al., 2020). Such simulations have even been used to predict optimal muscle behaviour in novel conditions, without performing any experiment (DeMers et al., 2017; Dorn et al., 2015; Ong et al., 2016). Similar models and simulations have also been made and analysed for a variety of other land vertebrates (Bishop, Michel, et al., 2021; Heers et al., 2018; Lerner et al., 2015; Schaffelhofer et al., 2015; see Demuth et al., 2023). In horses, biomechanical models have been used to estimate forces at the joints, muscles, tendons and ligaments during walking, trotting, galloping and jumping, at speeds up to 18 $\mathrm{m\,s^{-1}}$ (65 $\mathrm{km\,h^{-1}}$), and the results of these simulations overall are relatively consistent with experimental data (e.g. Becker et al., 2020; Harrison et al., 2010, 2012; Swanstrom et al., 2004). Biomechanical simulations have even been used to study the locomotion in extinct species, such as several non-avian dinosaurs, by reconstructing muscular parameters from muscular insertion scars on bones and comparisons with extant species (Anderson et al., 2023; Bates et al., 2010; Bishop, Cuff, et al., 2021; Bishop, Falisse, et al., 2021; Hutchinson et al., 2005; Sellers & Manning, 2007). Such methods could be very useful for estimating the loading of rhinoceros limbs.

The first step of musculoskeletal modelling and simulations is to define segments representing the different limb bones that can move relative to one another (Bishop, Cuff, et al., 2021; Seth et al., 2018). The joints between these bones are also defined. Muscles are modelled to act around those joints, able to generate moments. These moments must match the moments generated by a ground reaction force (GRF; usually estimated from body mass) for the system to be at static equilibrium, which is necessary for many inverse simulations, in which most motions and forces are prescribed input parameters, rather than outputs as in predictive simulations (e.g. Demuth et al., 2023). When an inverse simulation is run, the software calculates the optimal activation (and thus, force output) of each muscle necessary (usually, the sum of the squares of the activation of each muscle is minimised; Erdemir et al., 2007) to counteract the ground reaction force (i.e. maintain static equilibrium) or to generate movement in the case of a dynamic simulation (e.g. Bishop, Cuff, et al., 2021; Seth et al., 2018). The simulation procedure also calculates a joint reaction force, that is, a compressive force generated at each joint on each bone, which originates from segment and body mass properties (or the ground reaction force) and muscular contractions pulling the bones together.

Here, our aim is to estimate the 3D distribution of forces applied to the six long bones of the limbs of an adult white rhinoceros standing at rest and to use these forces to infer the potential morphofunctional adaptations of bone shape to forces imposed by muscles. To that end, we built a 3D musculoskeletal model of a forelimb and hindlimb using the muscle data collected by Etienne et al. (2021). We chose to model an immobile rhinoceros, as this corresponds to the most common loading conditions for rhino bones; and it is the simplest to model and simulate for an initial study. We expected to find that the limb extensor muscles would be the most active ones, as they counteract body weight (or, equivalently, generate ground reaction forces). Muscles with the largest moment arms should be more active in the simulation, as they can generate greater moments than muscles with shorter moment arms, even if generating the same forces.

2 | MATERIALS AND METHODS

2.1 | Creation of the model

We here follow the musculoskeletal modelling methodology and tools used by Bishop, Cuff, et al. (2021). The bones used for this study were digitised from computed tomography scans (0.60–0.82 mm transverse resolution, 2.5 mm longitudinal resolution, except pes and manus: 1.25 mm longitudinal resolution), using Avizo software (Thermo Fisher Scientific, 2019, Waltham, United States). The specimen was an adult female, the same as the adult white rhinoceros studied in Etienne et al. (2021), except for the pelvis, as that bone was not kept after the dissections. The pelvis comes instead from the Museos Natuurhistorisch Museum (Koksijde, Belgium; collection number MEO 2208e; adult female) and was digitised using a Creaform HandySCAN 300 surface scanner and VXElements (Creaform, Levis, Canada) and Geomagic Wrap 2017 software (3D Systems, Rock Hill, United States). It was scaled by a 1.1 factor for the femoral head to fit inside the acetabulum with an approximately 2 mm spacing, corresponding roughly to what we would expect for cartilage thickness there (Lee et al., 2014; Mancini et al., 2019). Each bone mesh was decimated to 50,000 faces.

Two separate models were created, one for each limb. We divided each limb into five different segments, each of which could move relative to one another. These were the scapula, humerus, radius-ulna, carpus-metacarpus and phalanges for the forelimb; and hemipelvis, femur, tibia-fibula, tarsus-metatarsus and phalanges for the hindlimb. We did not divide the phalanges into three different segments, as in rhinos the phalanges present flat articular areas with very reduced (if not completely absent) possibilities for flexion/extension at the interphalangeal joints (see Figure S1). The three digits of the manus and the pes were modelled as one, as in some other studies (Bishop, Cuff, et al., 2021; Bishop, Michel, et al., 2021). The patella was considered fixed to the femur, in the same approximate position as it is when the limb is in extension. A musculoskeletal model needs to clearly establish how the bones can move relative to one another. We created anatomical coordinate systems (ACSs) using both ends of each segment, defining three orthogonal axes of rotation corresponding to anatomical movements (flexion and extension, abduction and adduction, long-axis rotation), as per Bishop, Cuff, et al. (2021) and Gatesy et al. (2022) and references therein. Five of them were defined for each limb: four for the articulations (shoulder, elbow, wrist and metacarpophalangeal joints in the forelimb; hip, knee, ankle and metatarsophalangeal joints in the hindlimb), and a central one, positioned approximately between the two scapulae (forelimb) or between the two acetabula (hindlimb), which was used for positioning the whole limb.

To construct the above ACSs, the articular surfaces of all of the bones were cut out in Meshlab software (Cignoni et al., 2008), producing a mesh with only the proximal or distal articular surface (Figure 1a). Geometric primitives (spheres for the shoulder and hip; planes for the proximal tibia and the proximal part of the proximal phalanges; cylinders for the distal part of the humerus and femur, distal part of the tibia, proximal and distal parts of the radius-ulna and carpus-metacarpus and tarsus-metatarsus; Figure 1a,b) were fitted to the meshes of the articular surfaces, using MATLAB (R2020b, The MathWorks Inc, Natick, United States) script provided in Bishop, Cuff, et al. (2021). Primitives were chosen according to what corresponded best to the shape of the articular surfaces and the possibilities of movement of the joint (spheres for joints with three degrees of freedom, cylinders for joints restricted to a single rotation axis; the planes simply helped define proximal-distal axes). This procedure also estimated joint centres and axes of rotation. We created the ACSs in Rhinoceros software (v7, Robert McNeel and Associates, 2020, Seattle, United States; Figure 1b). Distances between two segments were generally constrained by the shapes of the intervening articulation. For instance, the position of the humerus relative to the scapula was estimated by superimposing the centre of rotation of each fitted sphere. In the case of the knee, the distance between the femur and tibia depended on the thickness of articular cartilage. We followed radiographs of the knee of a horse in Barone (2010) to approximate the proper distance. Variations in cartilage thickness are unlikely to affect the model results since articular cartilage is thin in mammals (Bonnan et al., 2013; Malda et al., 2013).

We also reconstructed the volume of soft tissues around each limb segment in Rhinoceros software, which provided us with segmental mass properties: mass, centre of mass and moments of inertia for each segment of the limb. Photos of the rhinoceros (the same specimen as the bones and muscle data, filmed before its death) in lateral, cranial and caudal views were imported directly into Rhinoceros, scaled and rotated to serve, for each segment, as a reference for the dimensions of the soft tissues around each segment of the limb, in the mediolateral and craniocaudal directions (Figure 1c). This created several ellipses, between two and four per segment, including ones at the borders with other

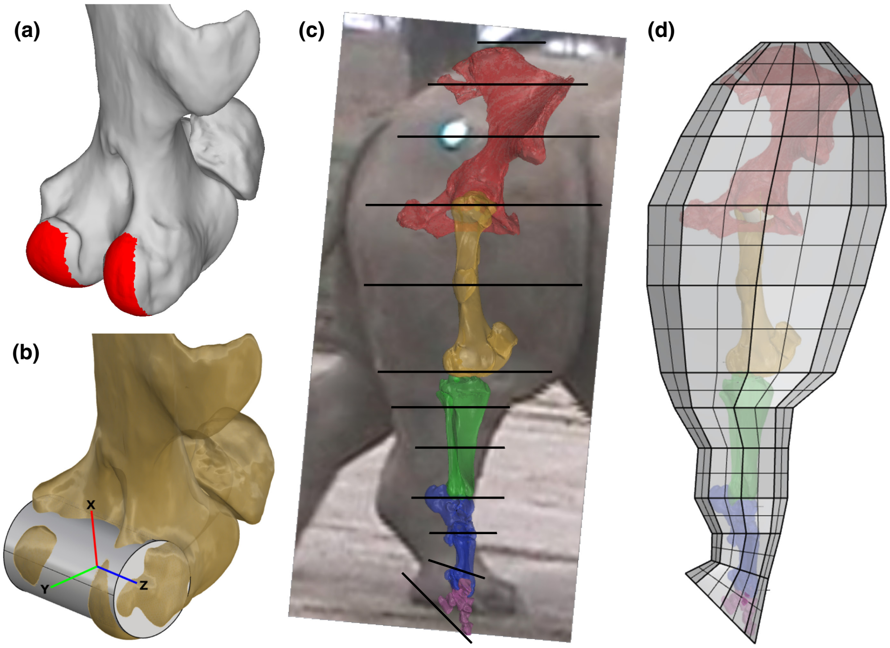

FIGURE 1 First steps in the creation of the rhinoceros musculoskeletal model. (a) Distal part of the femur, caudolateral view. Parts in red were cutoff from the mesh and used to fit a geometric primitive (here, a cylinder) representing the shape of the joint. (b) Distal part of the femur, caudolateral view. The cylinder has been generated from (a). An anatomical coordinate system (ACS) has been created, with its origin at the volumetric centroid of the cylinder, with the *Z* axis corresponding to the rotation axis of the cylinder (mediolateral), the *X* axis being effectively proximodistal and the *Y* axis being perpendicular to the other two (effectively craniocaudal). (c) Right hindlimb in lateral view, overlaid on a photograph of *Ceratotherium simum*'s hindlimb used to reconstruct the volume of each segment. The limb is shown straight (reference pose with joint angles at 0°), not in an anatomical position. The black lines indicate the major axis of the ellipses (perpendicular to the image and thus visible only as a line) used to determine the volumes of the fleshy segments. The photographs were rotated before defining the ellipses so that they fit each bone as well as possible. (d) Whole volume of the fleshy parts of the limb, as reconstructed from *Ceratotherium*.

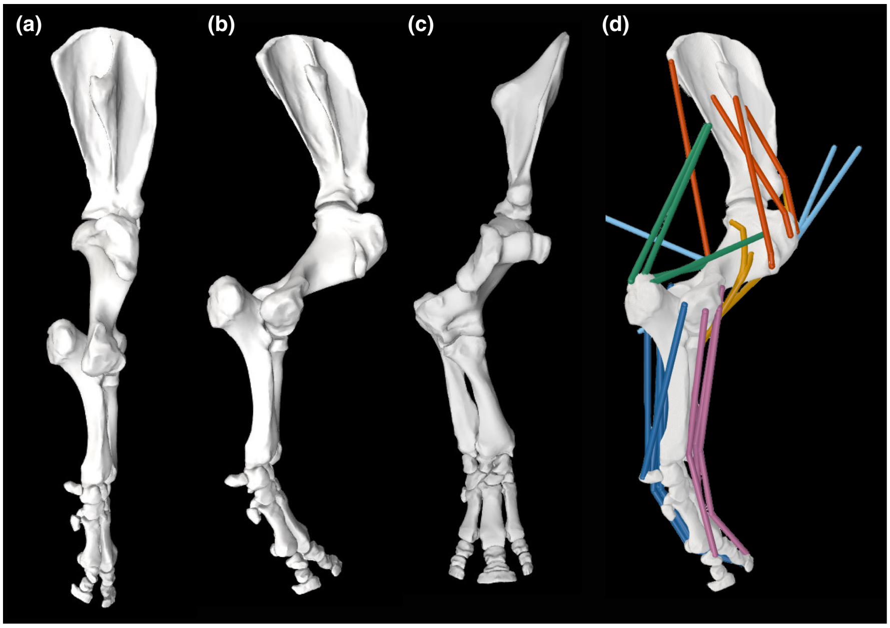

FIGURE 2 Final musculoskeletal model of the right forelimb. (a) Reference pose (all angles at 0°), lateral view. (b) Standing pose, lateral view. (c) Standing pose, cranial view. (d) Model from (b) with all muscle paths added. Colours according to muscle functional group as in Figure 3.

segments, depending on the complexity of the shape of the soft tissues. Segments with sharp changes in soft tissue shape required more ellipses. The ellipses were linked to create a closed mesh encompassing the soft tissues of each limb segment (Figure 1d). The ACSs, bone meshes and soft tissue meshes were imported into Autodesk Maya (Autodesk, 2022, San Francisco, United States) software to process them for conversion to an OpenSim musculoskeletal model via the custom MATLAB script provided by Bishop, Cuff, et al. (2021). The bone meshes exported from this process were decimated again, down to 10,000 faces, to reduce the computational time in OpenSim and because they are only used as visual aids (e.g. Seth et al., 2018). The soft tissue meshes were automatically used to provide a mass, centre of mass and moments of inertia for each segment and centre of mass coordinates were linked to the ACSs of their respective segments.

The ACSs positioned in the model allowed positioning of the limb, deviating from a 'reference pose' which defines all angles at 0° (straight vertical; Figure 2a), by modifying joint angles (e.g. increase humerus flexion by 10° and decrease tibial rotation by 5°). Each joint was restricted to only flexion/extension, except the most proximal ones (shoulder and hip), which retained three degrees of rotational freedom because they have ball-and-socket articulations (e.g. Harrison et al., 2010). All other joints had roughly cylindrical articulations with limited possibility for abduction/adduction or rotation. We set the pose for modelling and simulation to the approximate natural position of each limb when standing at rest. That position was determined by comparing photos and films of white rhinoceroses from various angles as well as some comparisons with mounted skeletons (Figure 2b,c). Screenshots of the OpenSim musculoskeletal model were overlayed on photographs of white rhinoceroses to estimate the position of each bone (Figure S2). The limb posture varies even when rhinos are standing still, notably in terms of limb protraction/retraction and mediolateral limb spacing; our chosen posture is a reasonable approximation. To further test the influence of limb posture on the results, a sensitivity analysis was performed where all joints were either flexed or extended by 10° and the resulting forces compared (see Data S1 for the results).

2.2 | Muscular data

Each muscle was then added to the musculoskeletal model (Figure 2d), using the Hill-type muscle model (Millard et al., 2013; Zajac, 1989). Muscle paths were reconstructed according to Etienne et al. (2021) and numerous photographs taken during those dissections. The simplest muscle paths were represented as straight lines from origin to insertion (e.g. *ulnaris lateralis*, *iliacus*). In more complicated cases, one or several 'via points' were included along the muscle's path, to avoid having muscles crossing through bones, and to ensure that the line of action was anatomically realistic (e.g. for the *supraspinatus*, *gluteus medius*). In the most complicated cases, where even via points would make the line of

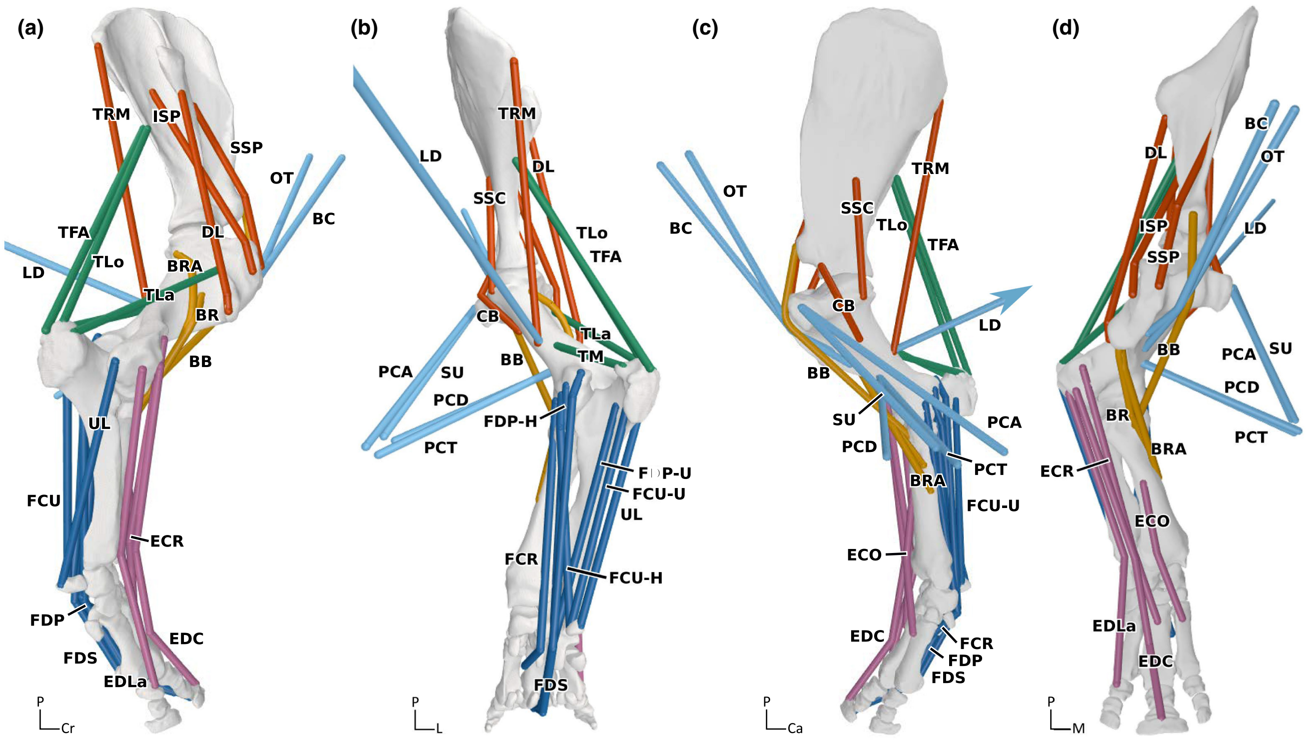

FIGURE 3 Musculoskeletal model of the forelimb, in standing at rest position, with paths of muscle-tendon units. Lateral (a), caudal (b), medial (c) and cranial (d) views. Muscles are coloured depending on their functional group, to help distinguish them (see Etienne et al., 2021). Muscle abbreviations are as in Table 1. Arrows indicate muscles that end outside of the visible area. P, proximal; M, medial; L, lateral; Cr, cranial; Ca, caudal.

action unrealistic, wrapping cylinders (Seth et al., 2018) were used (e.g. for the *biceps brachii*, *rectus femoris*). A total of 31 muscles were modelled in the forelimb (Figure 3) and 27 in the hindlimb (Figure 4). All the muscles described in Etienne et al. (2021) were included, except those observed not to act around the joints modelled here (e.g. the *serrati ventrales*), and the *fibulares*, due to their considered unclear homologies and low maximal force capacities. For each muscle, the moment arm in flexion/extension for all of the joints it crossed was recorded.

We input muscle fascicle lengths and pennation angles from the muscle architectural data presented by Etienne et al. (2021) into the model. The maximal isometric force-generating capacity of each muscle (F_{max}) was then added to the model, assuming 30 N cm^{-2} of PCSA, the PCSA values coming from Etienne et al. (2021). The adult *C. simum* used here was old for a rhinoceros (40 years old) and presented a generalised weakness at the end of its life. We thus decided to increase all F_{max} so that the total F_{max} was equal to that observed in the *R. unicornis* specimen from Etienne et al. (2021), which was of comparable body mass (2065 kg vs. 2160 kg). That specimen was also old when it died but did not present a generalised weakness, so we expected its muscles to provide more reliable data. This change resulted in an increase in the strength of the muscles by a factor of 1.41 for the forelimb and 1.75 for the hindlimb. These increases were equivalent to maximal muscle stress of up to 52.5 N cm^{-2} for the muscles of the hindlimb, which is still below the value used in several human models, in which ~60 N cm^{-2} is common (Arnold et al., 2010; Rajagopal et al., 2016).

2.3 | Inverse simulations

Each model was run in a static, standing-at-rest position (as above), using the static optimisation function in OpenSim (Seth et al., 2018). A GRF is applied, and the muscles activate, attempting to achieve static equilibrium (i.e. balance all moments around the limb joints; from the inverse dynamics function in OpenSim). The optimisation algorithm minimises the sum of the squares of the activation of all the muscles. Each limb was considered to bear a fraction of the total ground reaction force. In non-primate mammalian quadrupeds, the forelimbs typically bear 60% of the body weight of the animal (Alexander et al., 1979; Basu et al., 2019; Griffin et al., 2004; Witte et al., 2004), but no data are specifically available for rhinos. Using an admittedly simplified, crude 3D model of a rhinoceros (available here: https://www.turbosquid.com/3d-models/rhinoceros-rhino-3ds-free/1072005), we

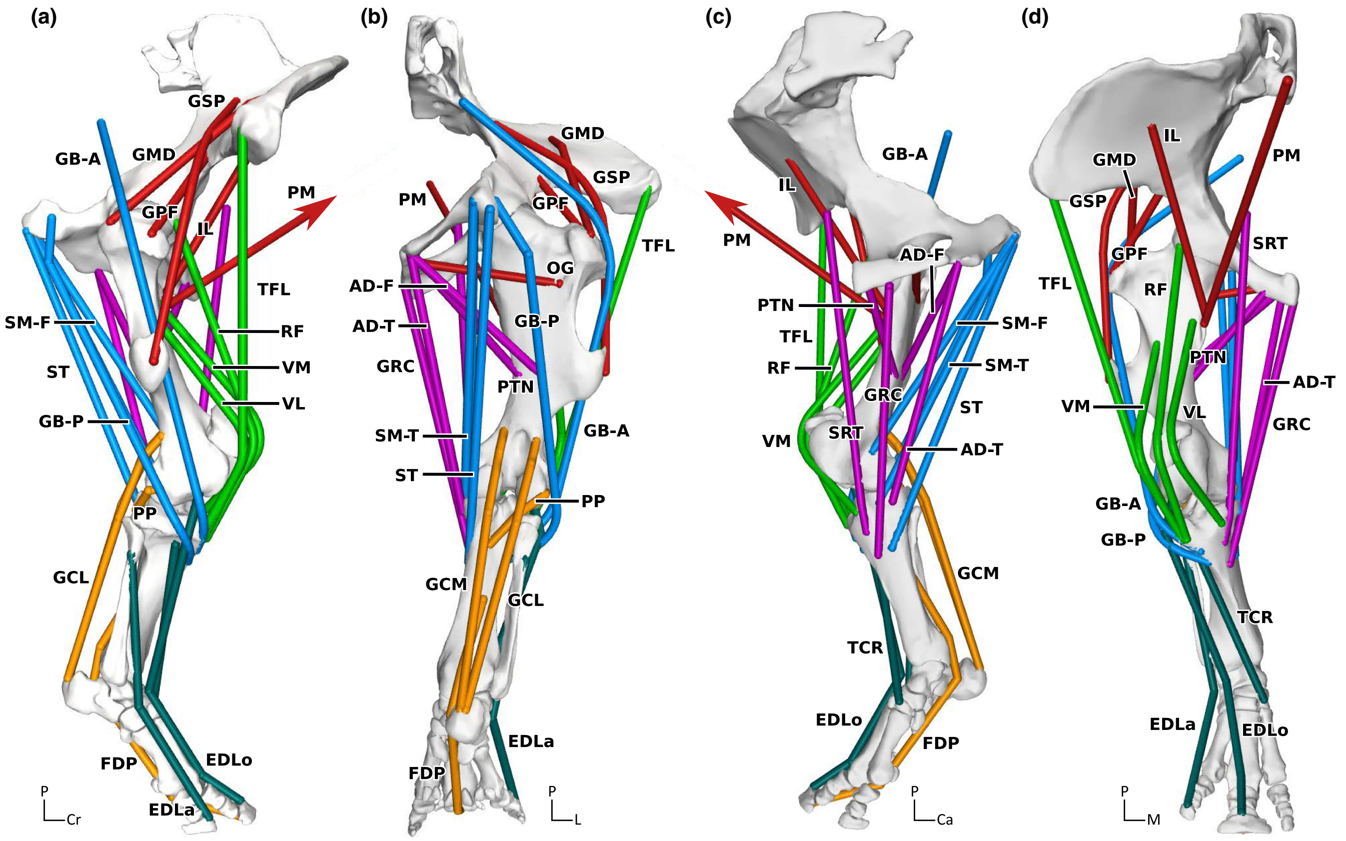

FIGURE 4 Musculoskeletal model of the hindlimb, in standing at rest position, with paths of muscle-tendon units. Lateral (a), caudal (b), medial (c) and cranial (d) views. Muscles are coloured depending on their functional group (see Etienne et al., 2021), to help distinguish them. Muscle abbreviations are as in Table 2. Arrows indicate muscles that end outside of the visible area. Ca, caudal; Cr, cranial; L, lateral; M, medial; P, proximal.

computed the position of the centre of mass in Blender (v2.81, 2019, Blender Foundation, Amsterdam, Netherlands), assuming a homogeneous density, and measured the craniocaudal moment arm of a vertical GRF applied at forefoot and hindfoot around the centre of mass. The model was slightly modified in Blender to correct excessive hindlimb retraction as compared with our standing posture. For the system to be balanced with a 60%:40% distribution of the GRF on the forelimb/hindlimb, the moment arm of the GRF around the centre of mass had to be 50% longer for the hindlimb than the forelimb. We found a 79% longer moment arm for the hindlimb, which would result in a 64%:36% distribution of body weight between the forelimb and hindlimb (Figure S3). We considered this close enough, particularly with the likely errors involved in these estimates, to the basic value of 60%:40% to justify our assumption that rhinos do not deviate from that value. Thus, a vertical GRF vector of 30% body weight was applied to the forelimb, and 20% to the hindlimb, corresponding to 6356.88 N and 4237.92 N, respectively, for the model's total mass of 2160 kg. We assumed that the GRF was purely vertical as a simplification since the animal was modelled as not accelerating. Empirical data on the direction of the GRF are surprisingly sparse for quadrupedal animals standing still; some data for cats indicate that there may be a medial component to the GRF, but it is very small compared to the vertical component (Macpherson, 1994). The GRF was applied to the digits, at the centre of pressure on the foot during midstance of a walking *C. simum*, following Panagiotopoulou et al. (2019), that is, near the base of the middle digit. The positions of the scapula and pelvis were locked in the simulation. The force–length relationships (sensu, e.g. Millard et al., 2013; Zajac, 1989) of the muscles were not taken into account; that is, muscle forces did not depend on the length of their fibres in the posture tested. This was necessary because OpenSim's static optimisation routine does not consider the stretching of the tendons; as a result, the muscles' fibres can be excessively stretched, thus lowering their possible force output if we used the force–length relationships (Heers et al., 2018). No 'reserve actuators' were used, except on the most proximal ACS (at the top of the chain; three forces (maximum 10,000 N) and three moments (maximum 10,000 N m) from 'residual actuators') to compensate for the GRF (and missing forces such as those from the remainder of the body) and avoid the whole model moving upwards (see Hicks et al., 2015; Seth et al., 2018). Joint reaction forces were extracted using the JointReaction function in OpenSim's Analysis tool. These forces included forces related to the ground reaction force itself (and segmental inertial properties), and forces originating from the compression that muscles exert indirectly on the joints, by pulling the bones together.

3 | RESULTS

Here we present outputs of the model for the moment arms of limb muscle-tendon units, then muscle activations output by the inverse simulation and then finally, the joint reaction forces from that simulation.

3.1 | Forelimb model and simulation outputs

The *biceps brachii* (BB), *brachiocephalicus* (BC), *omotransversarius* (OT) and *supraspinatus* (SSP) muscles had the longest moment arms in shoulder extension (between 11 and 13 cm, Table 1, Figure 7). The *tensor fasciae antebrachiae* (TFA) and all heads of the *triceps brachii* had the longest moment arms in elbow extension (between 9 and 16 cm). The *ulnaris lateralis* (UL) and *flexor carpi ulnaris* (FCU) had the longest moment arms in wrist plantarflexion (~6 cm). The *flexores digitorum superficialis* (FDS) and *profundus* (FDP) had the longest moment arms in digit plantarflexion (3–4 cm).

The *latissimus dorsi* (LD), *tensor fasciae antebrachiae*, *teres major* (TRM), and long head of the *triceps brachii* (TLo) had the longest moment arms in shoulder flexion (between 10 and 20 cm). The *biceps brachii*, *brachialis* (BR), and *brachioradialis* (BRA) had the longest moment arms in elbow flexion (~7 cm). The *extensor digitorum communis* (EDC) had the longest moment arm in wrist and digit dorsiflexion (6.4 and 3.6 cm, respectively).

The most active muscle of the forelimb was the *ulnaris lateralis*, exerting 0.80 of its maximal isometric force (simulated muscle activation varies between 0.01 [minimal activation; 1%] and 1 [maximal activation; 100%]; Table 1, Figure 5). It was three times more active than the second most active muscle, the *flexor digitorum superficialis*, and exerted a force 3.6 times greater than the muscle with the second-highest exerted force, the *supraspinatus* (9239 N vs. 2538 N, 44% vs. 12% of body weight). Eight muscles exerted more than 1000 N (Table 1): the *ulnaris lateralis*, *pectoralis descendens* (PCD), *flexor digitorum superficialis*, *triceps brachii* (lateral head, TLa), *subscapularis* (SSC), *supraspinatus*, *flexor digitorum profundus* (ulnar head, FDP-U), and *biceps brachii*. Conversely, 12 muscles were only active at 0.01 of their F_{max}, corresponding to the minimal simulated activity: *extensor carpi obliquus* (ECO), *brachioradialis*, *teres major*, *brachialis*, *extensor digitorum lateralis* (EDLa), *extensor digitorum communis*, *extensor carpi radialis* (ECR), *tensor fasciae antebrachii*, *deltoideus* (DL), *infraspinatus* (ISP), *latissimus dorsi* and *triceps brachii* (long head).

The joint reaction forces for the forelimb mainly were oriented in a proximodistal direction (Figure 5), with 7741 N (37% of body weight; BW) at the shoulder, 14,835 N (70% BW) at the elbow, 14,373 N (68% BW) at the wrist and 2532 N (12% BW) at the metacarpophalangeal joint. Reserve (residual) actuators for the scapula/body were 5376 N in the ventral direction (84.6% of GRF applied) for translation and for rotation 104, 1500 and 285 N m in retraction (extension), adduction, and external rotation (respectively 4.57%, 66.1% and 12.5% of GRF times the height of the scapula segment's centre of mass [1.19 m]).

3.2 | Hindlimb model and simulation outputs

The caudal part of the *gluteobiceps* (GB-P), the *semitendinosus* (ST), and the *semimembranosus* (SM) muscles had the longest moment arms in hip extension (between 16 and 19 cm, Table 2, Figure 7). The *tensor fasciae latae* (TFL) and all heads of the *quadriceps femoris*

TABLE 1 Results from modelling and simulating the forelimb.

		Force			Moment arms			
Muscle	Abb.	F_{max}	F	Act.	Shoulder	Elbow	Wrist	MCP
Supraspinatus	SSP	11,486	2538	0.22	−11.3			
Subscapularis	SSC	6989	1073	0.15	2			
Coracobrachialis	CB	2831	133	0.05	−1.6			
Infraspinatus	ISP	16,131	161	0.01	−6.2			
Brachiocephalicus	BC	1424	114	0.08	−12.9			
Omotransversarius	OT	1196	94	0.08	−13.1			
Deltoideus	DL	5810	58	0.01	−0.2			
Latissimus dorsi	LD	18,549	186	0.01	13			
Teres major	TRM	497	5	0.01	11.7			
Pectoralis descendens	PCD	4230	1088	0.26	−4.3			
Pectoralis transversus	PCT	2624	243	0.09	1.3			
Pectoralis ascendens	PCA	3934	294	0.07	4			
Subclavius	SU	3934	135	0.03	5.2			
Biceps brachii	BB	11,378	1381	0.12	−12.5	7.1		
Brachialis	BR	1539	16	0.01		7.3		
Brachioradialis	BRA	123	1	0.01		7.6		
Triceps brachii (lateral head)	TLa	4738	1059	0.22		−11.2		
Triceps brachii (long head)	TLo	20,291	203	0.01	19.5	−14.4		
Triceps brachii (medial head)	TM	2057	164	0.08		−9.2		
Tensor fasciae antebrachii	TFA	3545	36	0.01	20.7	−16		
Ulnaris lateralis	UL	11,568	9239	0.8		−5.5	−6.3	
Flexor digitorum profundus (ulnar head)	FDP-U	6185	1319	0.21			−3.4	−3.5
Flexor digitorum superficialis	FDS	3871	1088	0.28		−5.3	−5.2	−4.3
Flexor carpi ulnaris (humeral head)	FCU-H	1738	151	0.09		−2	−5.6	
Flexor carpi ulnaris (ulnar head)	FCU-U	1738	136	0.08			−6.1	
Flexor carpi radialis	FCR	806	21	0.03		0.1	−4.5	
Flexor digitorum profundus (humeral head)	FDP-H	356	7	0.02		−2.9	−3.7	−3
Extensor carpi radialis	ECR	3877	39	0.01		4.4	4.8	
Extensor digitorum communis	EDC	2681	27	0.01		3.6	6.4	3.6
Extensor digitorum lateralis	EDLa	2251	23	0.01		0	4.2	−1.2
Extensor carpi obliquus	ECO	102	1	0.01			4.4	

Note: Forces are in Newtons. Moment arms, expressed in centimetres, are calculated for the flexion/extension action with the limb in a standing position. Negative moment arms, in blue, indicate an antigravity action and positive moment arms, in red, the opposite. Colour intensity follows value intensity.

Abbreviations: Act., activation in the simulation; F, force output in the simulation; F_{max}, maximal isometric force-generating capacity; MCP, metacarpophalangeal.

had the longest moment arms in knee extension (between 7.5 and 10 cm). The *gastrocnemius* had the longest moment arm in ankle plantarflexion (~9 cm). The *flexor digitorum profundus* (FDP) had the longest moment arm in digit plantarflexion (3 cm).

The *tensor fasciae latae*, *sartorius* (SRT) and *psoas major* (PM) had the longest moment arms in hip flexion (between 12 and 16 cm, Table 2). The *semitendinosus* and *gastrocnemius* had the longest moment arms in knee flexion (between 6 and 8.5 cm). The *extensor digitorum longus* (EDLo) and *lateralis* and the *tibialis cranialis* (TCR) had similar moment arms in ankle dorsiflexion (between 4.75 and 6.25 cm). The *extensor digitorum longus* had the longest moment arm in digit dorsiflexion (2.7 cm).

The most active muscle of the hindlimb was the lateral head of the *gastrocnemius* (GCL), exerting 0.56 of its maximal isometric force (Table 2, Figure 6). It was more than twice as active as the second most active muscle, the medial head of the *gastrocnemius*

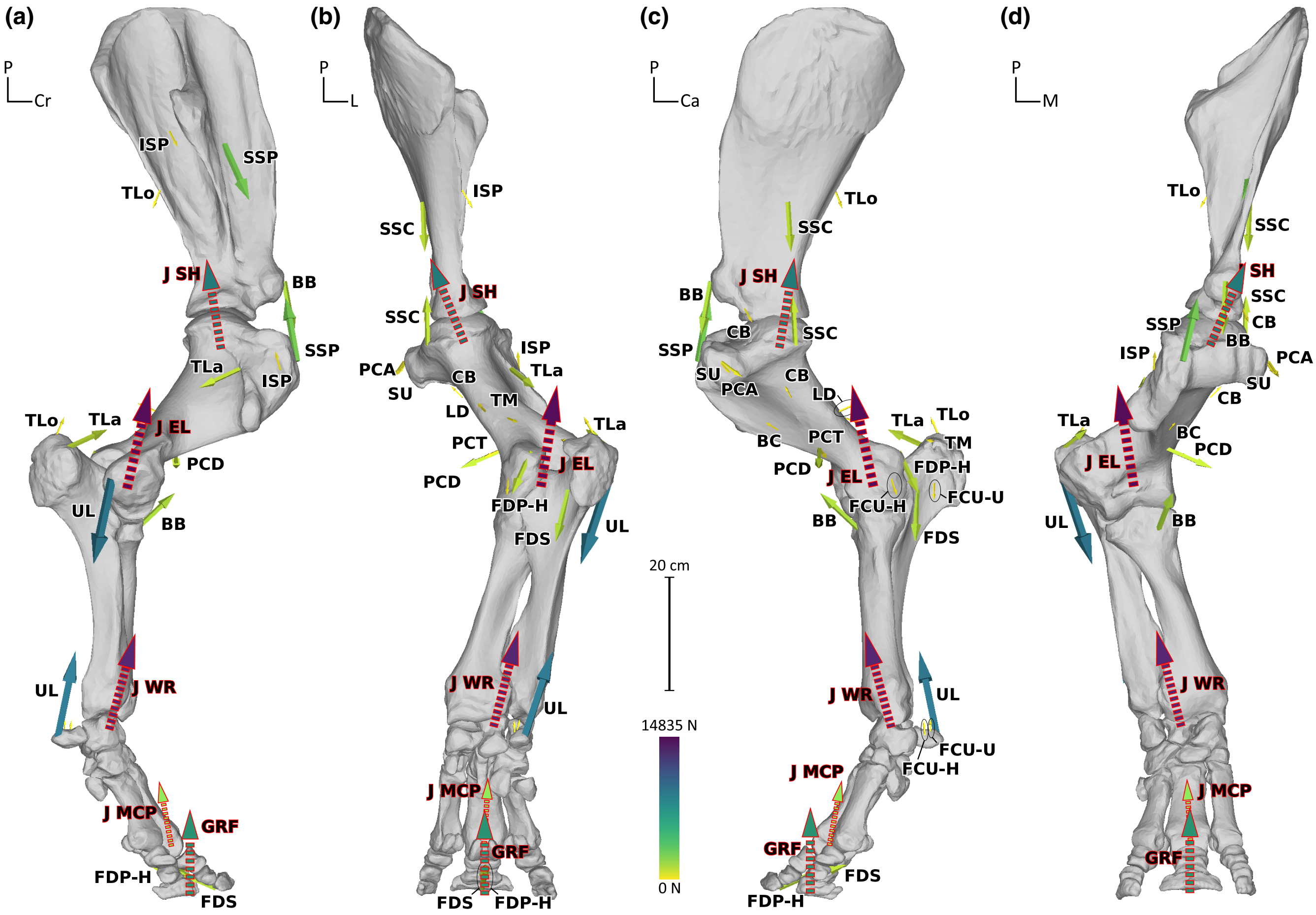

FIGURE 5 Force vectors input for (GRF), and output by (muscles, joint reactions), from the inverse simulation of the forelimb. Lateral (a), caudal (b), medial (c) and cranial (d) views. Only forces above 100 N are shown; arrow length is proportional to the natural logarithm of the force exerted. The reaction forces are outlined in red and shown originating at the centre of each joint (or, for GRF, third digit): ground reaction force (GRF), and joint reaction forces at the: elbow (J EL), shoulder (J SH), metacarpophalangeal joint (J MCP) and wrist (J WR). Muscle abbreviations are as in Table 1. Ca, caudal; Cr, cranial; L, lateral; M, medial; P, proximal.

(GCM) and exerted a force 1.74 times greater than the muscle with the second-highest exerted force, the *flexor digitorum profundus* (4908 N vs. 2824 N, 23% vs. 13% BW). Five muscles exerted more than 1000 N: the lateral head of the *gastrocnemius* (GCL), both parts of the *gluteobiceps*, the *gluteus medius* (GMD), and the *flexor digitorum profundus*. Fourteen muscles were only active at 0.01 of their F_{max}, corresponding to the minimal simulated activity (Table 2): the *gluteus profundus* (GPF) and *superficialis* (GSP), *psoas major*, *illiacus* (IL), *gracilis* (GRC), *obturator et gemelli* (OG), *adductors* (both parts, AD-F and AD-T), *sartorius*, *pectineus* (PTN), *popliteus* (PP), *extensor digitorum longus*, *tibialis cranialis* and *extensor digitorum lateralis* (EDLa).

The joint reaction forces for the hindlimb were also mainly oriented in a proximodistal direction, with 6608 N (31% BW) at the hip, 13,038 N (62% BW) at the knee, 11,195 N (53% BW) at the ankle, and 2806 N (13% BW) at the metatarsophalangeal joint. Reserve (residual) actuators for the pelvis/body were 2142 N in the ventral direction (50.5% of GRF applied), and 313, 33 and 12 N m in retraction (extension), abduction and external rotation (respectively 6.1%, 0.23% and 0.63% of GRF times the height of the pelvis segment's centre of mass [1.21 m]).

4 | DISCUSSION

In this study, we used two 3D musculoskeletal models in static simulations to estimate what the muscular and joint reaction forces were in the major fore- and hindlimb joints of a standing rhinoceros. Now we first consider what our findings mean for our main questions; that is, were the limb extensor muscles the most active, and were muscles with the largest moment arms about a given degree of freedom the most active? We then contemplate the importance of co-activation of antagonistic muscles at certain joints, of passive support mechanisms and of the reserve actuators that our simulation opted to activate to balance the proximal forces and moments. Last, we reflect on how the muscles seemed to load the bones in our simulations.

4.1 | Muscle and actuator activation patterns

4.1.1 | Proximal limb segments

Consistent with our prediction, the muscles delivering the greatest forces were antigravity muscles (extensors of the arm, forearm, thigh

TABLE 2 Results from modelling and simulating the hindlimb.

		Force			Moment arms			
Muscle	**Abb.**	F_{max}	*F*	**Act.**	**Hip**	**Knee**	**Ankle**	**MTP**
Gluteus medialis	GMD	11,363	1163	0.1	−2.9			
Gluteus profundus	GPF	5653	75	0.01	2.7			
Gluteus superficialis	GSP	5256	57	0.01	7.2			
Psoas major	PM	6050	61	0.01	12.4			
Iliacus	IL	3857	39	0.01	8.6			
Gluteobiceps (caudal part)	GB-P	8576	1973	0.23	−17	1.9		
Semitendinosus	ST	5316	402	0.08	−19.2	8.5		
Semimembranosus (femoral insertion)	SM-F	2654	159	0.06	−16.3			
Semimembranosus (tibial insertion)	SM-T	2654	129	0.05	−17.6	3.6		
Gluteobiceps (cranial part)	GB-A	6527	1125	0.17	−3.6	−4.4		
Gracilis	GRC	4926	49	0.01	3.1	1.7		
Obturator et gemelli	OG	6195	63	0.01	0			
Adductores (femoral insertion)	AD-F	1261	16	0.01	−7.2			
Adductores (tibial insertion)	AD-T	1261	14	0.01	−9.9	4.9		
Sartorius	SRT	787	8	0.01	14	−3.1		
Pectineus	PTN	591	6	0.01	7.3			
Vastus lateralis	VL	6167	597	0.1		−9		
Vastus medialis	VM	5008	326	0.07		−7.5		
Rectus femoris	RF	5510	284	0.05	5.9	−10.1		
Tensor fasciae latae	TFL	11,233	577	0.05	15.8	−9		
Gastrocnemius (lateral head)	GCL	8756	4908	0.56		5.8	−8.8	
Flexor digitorum profundus	FDP	16,703	2824	0.17			−4.7	−3
Gastrocnemius (medial head)	GCM	3687	871	0.24		6.1	−8.9	
Popliteus	PP	808	9	0.01		1.1		
Extensor digitorum longus	EDLo	2972	30	0.01		−5.3	5.9	2.7
Tibialis cranialis	TCR	1270	13	0.01			6.3	
Extensor digitorum lateralis	EDLa	435	5	0.01			4.8	1.5

Note: Forces are in Newtons. Moment arms, expressed in centimetres, are calculated for the flexion/extension movement with the limb in a standing position. Negative moment arms, in blue, indicate an antigravity action and positive moment arms, in red, the opposite. Colour intensity follows value intensity.

Abbreviations: Act., activation in the simulation; *F*, force output in the simulation; F_{max}, maximal isometric force-generating capacity; MTP, metatarsophalangeal.

and lower leg joints; plantar flexors of the manus, pes and digits; Figure 7, Tables 1 and 2) with long moment arms (e.g. 2538 N with a 11.3 cm moment arm in shoulder extension for the *supraspinatus* [0.22 activation, 12% BW], 1059 N and 11.2 cm in elbow extension for the lateral head of the *triceps brachii* [0.22, 5% BW], 1973 N and 17 cm in hip extension for the caudal *gluteobiceps* [0.23, 9% BW], and 597 N and 9 cm in knee extension for the *vastus lateralis* [VM; 0.1, 3% BW]; Tables 1 and 2, Figures 5 and 6). Several active muscles were both extensors of one joint and flexors of another, but their moment arm in extension was always longer than their moment arm in flexion (Figure 7), meaning that their flexion movement could be counterbalanced by other extensors. This multiarticular action was most notably the case with the *biceps brachii*, a strong extensor of the shoulder because of the great development of the supraglenoid tubercle in rhinoceroses (1381 N output [0.12 activation, 7% BW], 12.5 cm moment arm in shoulder extension, 7.1 cm in elbow flexion; Figure 7). Its action in elbow flexion was counterbalanced by the lateral head of the *triceps* and by the *ulnaris lateralis*. This was also the case for the *semitendinosus* (402 N [0.08, 2% BW], 19.2 cm in hip extension and 8.5 cm in knee flexion) and for the *gastrocnemius* (5779 N in total [0.46, 27% BW], ~6 cm in knee flexion and ~9 cm in ankle plantarflexion), which produced moments in knee flexion that were all counterbalanced by the extensor moments produced by the various heads of the *quadriceps femoris* (*vastus lateralis*, *vastus medialis*, *rectus femoris* [RF]), the *tensor fasciae latae* (TFL) and the cranial *gluteobiceps*. In the forelimb, adductors of the shoulder also delivered relatively large forces (e.g. 1073 N [0.15 activation, 5% BW] delivered for the *subscapularis*, 1088 N [0.26, 5% BW] for the

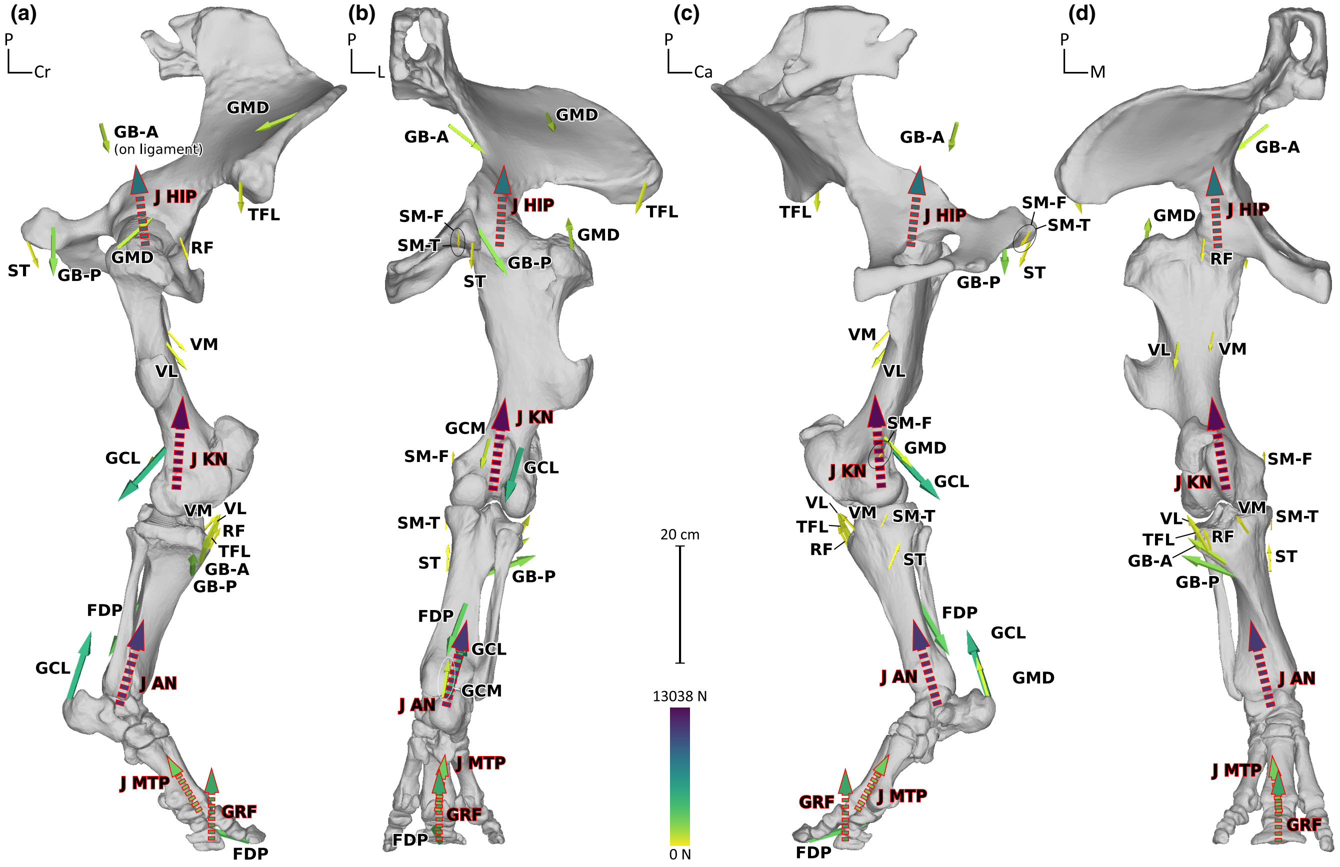

FIGURE 6 Force vectors input for (GRF), and output by (muscles, joint reactions), from the inverse simulation of the hindlimb. Lateral (a), caudal (b), medial (c) and cranial (d) views. Only the forces above 100 N are shown, arrow length is proportional to the natural logarithm of the force exerted. Outlined in red are the reaction forces, which are shown originating at the centre of each joint: ground reaction force (GRF), joint reaction force at the metatarsophalangeal joint (J MTP), joint reaction force at the ankle (J AN), joint reaction force at the knee (J KN), joint reaction force at the hip (J HIP). Muscle abbreviations as in Table 2. Ca, caudal; Cr, cranial; L, lateral; M, medial; P, proximal.

pectoralis descendens), due to the posture of the limb causing a large moment for shoulder abduction. In the hindlimb, there was a large moment for hip adduction, compensated mainly by the cranial *gluteobiceps* (1125 N, 0.17 activation, 5% BW; 17.9 cm moment arm in hip abduction, 3.6 cm in hip extension), along with the *gluteus medius* (GMD; 1163 N, 0.1, 5% BW, 6.1 cm in hip abduction and 2.9 cm in hip extension).

4.1.2 | Distal limb segments

Unlike the proximal parts of the limbs, in which muscles acting over two joints will often have an antigravity action around only one joint, the distal parts of the limbs often present muscles with an antigravity action around several joints. Such muscles were thus effective in supporting standing, even if their moment arms were shorter than in the proximal parts of the limbs. These muscles included the most active muscle of our sample, the *ulnaris lateralis* (9239 N output [0.8 activation, 44% BW], ~6 cm moment arm in elbow extension and wrist plantar flexion; Figure 7), but also the *flexores digitorum* of the forelimb (2414 N [0.23, 11% BW] output in total, 3.4–5.3 cm moment arm in elbow extension and wrist and digit plantarflexion) and hindlimb (2824 N [0.17, 13% BW], 4.7 cm in ankle plantarflexion, 3 cm in digit plantarflexion). The large moment arm of the *ulnaris lateralis* for elbow extension was due to the great caudo-distal development of the lateral epicondyle of the humerus in large rhinos (compare Figure 1d,e in Mallet et al., 2019; see also Figure 5a). This particular anatomical feature is not observed in smaller rhinoceroses (*Dicerorhinus sumatrensis*), nor in other perissodactyls, bovids and even hippopotamuses or elephants (Bader et al., 2022; Barone, 1999; CE, personal observation; Maclaren et al., 2018). Accordingly, data in horses do not indicate very strong activation of the *ulnaris lateralis* during locomotion (Harrison et al., 2010). This may be due to the absence of this large lever arm for elbow extension, making it less relevant for antigravity action, particularly as our static optimisation analysis automatically favours activating the muscles with the greatest antigravity moment-generating capacity. However, simulations involving static (i.e. inverse as here) optimisation and more dynamic optimisation tend to produce similar results (e.g. Anderson & Pandy, 2001), at least for slower locomotion. Obtaining empirical data on muscle excitation patterns (electromyography) in rhinoceroses to test the high activation of the *ulnaris lateralis* would be extremely difficult.

(a) - Muscular moment arm vs activation in the model for the forelimb

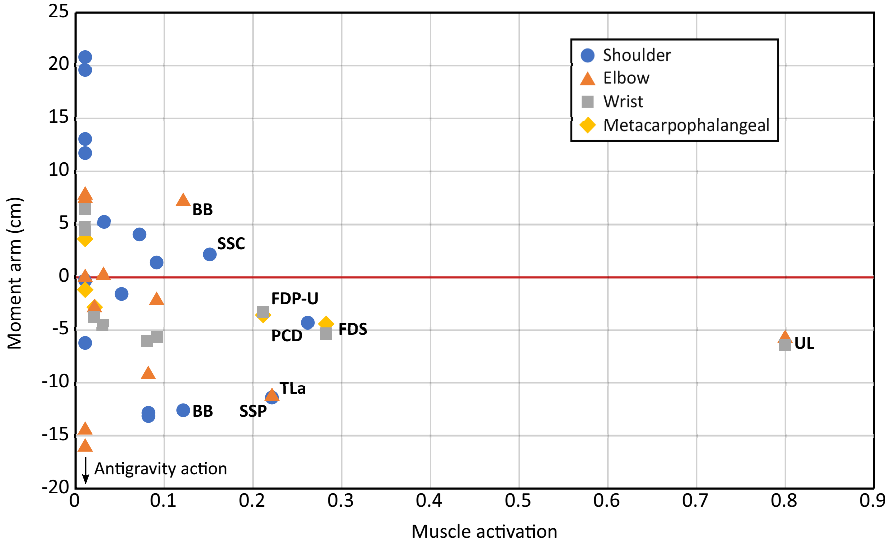

(b) - Muscular moment arm vs activation in the model for the hindlimb

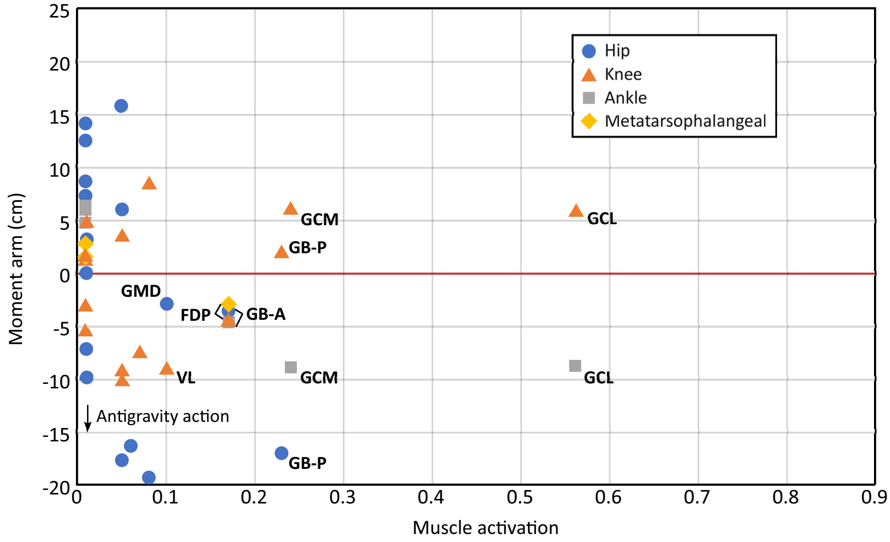

FIGURE 7 Relationship between muscular moment arm in flexion/extension around the different joints and activation, in the forelimb (a) and hindlimb (b). Acronyms for the muscles are in Tables 1 and 2.

4.1.3 | Co-contraction of antagonistic muscles

In our modelling, we have considered that muscles only contract (i.e. generate opposite moments) in order to counteract the moments created by the ground reaction force/body weight (and sometimes, moments created by other muscles, as in the case of the *gastrocnemius* and *quadriceps femoris* described above). However, it has been empirically observed in horses that antagonistic muscles (e.g. extensors and flexors of the digits) can co-contract, thus both generating more than the strictly necessary moments and compensating for one another (Harrison et al., 2012). Such behaviour can increase stability at the joints by preventing uncontrolled movements and has been observed during locomotion, especially during the transition from the swing phase to the stance phase (Harrison et al., 2012). In the absence of empirical data on rhinoceros muscle activation, it is impossible to conclude what the degree of co-contraction might be, especially when standing still. We could expect several muscles to show co-contraction in rhinos, for instance, the *biceps brachii* and *triceps brachii* (antagonistic over two joints, the shoulder and elbow; co-contraction could stabilise both joints against extension/flexion), or the pectorals and the *deltoideus* and *infraspinatus* (stabilisation of the shoulder against mediolateral movements) (Barone, 2010; Harrison et al., 2010, 2012). Because the hindlimb has a propulsive role, contributing relatively less to weight support than the forelimb, it might need less stabilisation via co-contraction. Overall, co-contraction of antagonistic muscles would increase muscular force outputs and thus joint reaction forces; thus, these forces may have been underestimated in our models.

4.1.4 | Passive support mechanisms

Although our simulations only allow for active muscle contraction to provide antigravity support for the joints, passive mechanisms are also likely, which would help keep the joints extended with reduced muscle forces required (e.g. Hermanson & Macfadden, 1996). In the knees of horses, the development of a medial ridge of the femoral and patellar trochlea creates a notch in which patellar ligaments can be constrained, thus locking the patella (and thereby the knee) into a position providing greatly reduced activity of the *quadriceps femoris* (Schuurman et al., 2003). Femoral and patellar anatomy suggest that passive locking of the knee exists in rhinos as well, although the exact organisation of the mechanism might be different in rhinos and horses, as tapirs do not seem to possess such a locking mechanism (Hermanson & Macfadden, 1996; Shockey, 2001). This locking mechanism would reduce the force output of each component of the *quadriceps femoris* (the *rectus femoris*, *vastus lateralis* and *vastus medialis*) as well as the joint reaction force at the knee. Other passive-stay apparatus exist in horses, although they are less well-documented, and may exist in rhinos (Hermanson & MacFadden, 1992; Mallet et al., 2019, 2021; Schuurman et al., 2003). For example, the great development of the intermediate tubercle of the humerus at the shoulder of horses increases the moment arm of the *biceps* for shoulder extension, and the very strong tendon of the *biceps* helps to passively produce a shoulder moment. That development of the intermediate tubercle is also present in large rhinos like *C. simum* and could serve the same mechanical function (Hermanson & MacFadden, 1992; Mallet et al., 2019, 2021). It is likely that rhinos would greatly benefit from such mechanisms, but a quantitative answer on how this could reduce the necessary muscular forces would require extensive in vivo and ex vivo experiments. Otherwise, the force that is applied actively by muscular contractions or passively by tendon/ligament resistance does not necessarily change its point of application or intensity, especially at the shoulder.

4.1.5 | Reserve actuator outputs

The force and moment outputs of the reserve (residual) actuators were much greater than those that would be recommended for typical musculoskeletal models (forces <5% GRF; moments <1% of COM height times GRF; see Hicks et al., 2015). This was likely due to the partial nature of the body segments analysed here. In particular, the GRF's external forces and moments were not balanced in the simulation by the whole body and other limbs. Only simplified abstractions of the mass properties of the scapular and pelvic regions (100 kg for the forelimb, 213.7 kg for the hindlimb) provided forces vs. 30% (648 kg) and 20% (432 kg) of the mass of the rhinoceros that would be supported by each forelimb and hindlimb, respectively, helping to explain the activations of those actuators. The actuators in translation corresponded to the 'missing' forces that must balance other forces originating ultimately from the GRF; the total weights of the forelimb (~981 N) and hindlimb (~2097 N) plus their reserve actuator (ventrally oriented) forces were equal and opposite to the (solely vertical/dorsally oriented) GRF. Similarly, in the forelimb, the actuator's 1500 N m adduction moment would not have been necessary if both right and left forelimbs were modelled, as their opposing moments should cancel out limb abduction. A model of the complete rhinoceros likely would not have these problems, but lies beyond the scope of this study, in the absence of data for the axial muscles of a rhinoceros incorporated into a rigorous whole-body model and simulation. Moreover, the absence of a clavicle in rhinoceroses (and in most Euungulata) means that the forelimb is only connected to the rest of the skeleton via soft tissues, which is challenging to model.

4.2 | Forces on the long bones

4.2.1 | Humerus

Our simulations estimated that the humerus is subjected to many forces, both compressive and tensile, in various directions (Figure 5, Table 1). With the rhino simulated standing at rest, forces totalled 40,532 N (191% BW), of which 22,576 N (107% BW) arose from joint reaction forces (7741 N at the shoulder, 14,835 N at the elbow) and 17,956 N (85% BW) came from muscle tension. Several of those muscles have insertion areas that are more developed in heavier than in lighter rhinos, consistent with our results. For example, the greater tubercle for the *supraspinatus* is enlarged, and the epicondyles for the *ulnaris lateralis* and *flexor digitorum superficialis* are as well (Mallet et al., 2021). It is likely that the *biceps*, despite not inserting on the humerus, also exerts a compressive force at the bicipital groove when contracting, as it wraps over it (see Figure 3c). Some areas are exceptions. Notably, the lesser tubercle (insertion of the deep pectorals; Etienne et al., 2021) is greatly developed in larger rhinos, but we did not find particularly high forces at that location; perhaps the deep pectorals are more active during locomotion to stabilise the limb. The joint reaction forces are not aligned with the long axis of the humerus, which is coherent with its marked inclination compared with the proximodistal axis of the whole forelimb.

4.2.2 | Radius and ulna

The total forces exerted on the radius and ulna respectively will depend on how the joint reaction forces are divided between the two bones. We assumed that the joint reaction force at the wrist would be spread evenly over the entire contact area between the radius and ulna and the carpal bones. This would give 73% of the joint reaction force to be borne by the radius and 27% by the ulna (the surface area of the radial contact with the carpal bones is 53.5 cm^2, and the surface area of the ulnar contact is 20.3 cm^2). We used the same ratio for the elbow's joint reaction force, as the partitioning of the joint reaction forces at the elbow is difficult to estimate due to the radius and ulna wrapping all around the humeral trochlea. This is consistent with the radius being the most weight-bearing bone of the forelimb zeugopodium in most quadrupedal mammals, due to its more cranial position, directly under the humeral trochlea (Bertram & Biewener, 1992). In addition to joint reaction forces at the elbow and wrist, the radius and ulna are probably subject to joint reaction forces from one another, as they are not fused in rhinos. Those could come from joint forces at the elbow and wrist, or from muscles and ligaments pulling the bones together.

The radius was subjected to 21,322 N (101% BW) in our simulation (Figure 5, Table 1). Almost all of this arose from compressive forces at the contact areas, nearly perfectly aligned with the long axis of the bone (10,830 N at the elbow, 10,492 N at the wrist, respectively 51% and 50% BW). 1399 N (7% BW) came from muscle tension, the vast majority (1381 N) from the *biceps brachii* alone, on the radial tuberosity. Mallet et al. (2021) reported a pronounced development of radial tuberosity in rhinoceroses with a greater body mass, which is consistent with a key stabilisation role for the *biceps* in heavy rhinos. If there is indeed co-contraction of the *biceps* and the *triceps* to stabilise the elbow when standing at rest, then the force from the *biceps* would be greater. This loading pattern is consistent with the general shape of the radius, which is that of a column, well suited to sustain great compressive loads (Bertram & Biewener, 1992), with few areas for the attachment of strong muscles; unlike, for example, the humerus.

The ulna was subjected to 10,803 N (51% BW) in our simulation (Figure 5, Table 1). Joint reaction forces amounted to 4005 N at the elbow and 3881 N at the wrist (respectively 19% and 18% BW). 2917 N (14% BW) arose from muscular forces. Again, it is likely that muscular forces at rest were underestimated, as co-contraction is expected. If the *triceps brachii* exerted its maximal force output it could deliver up to 27,086 N (128% BW), 20 times its output when standing at rest. This is likely close to the case during high-speed locomotion, when the *triceps* should be most active according to data in horses, to decelerate the limb at the end of the swing phase and to stabilise it during the stance phase (e.g. Harrison et al., 2012; Hodson-Tole, 2006; Watson & Wilson, 2007). The ulnar diaphysis is more robust in heavier rhinos (*C. simum*, *Rhinoceros unicornis*) than in smaller ones (*D. sumatrensis*), supporting the idea of an increased force output by the *triceps* in heavier species to provide better stabilisation and extension of the elbow (Mallet et al., 2019).

4.2.3 | Femur

Similar to the humerus, the femur was subjected to many different forces, due to the presence of many muscular insertions; totalling 28,026 N (132% BW): 6608 N from the joint reaction forces at the hip (31% BW), 13,038 N from the joint reaction forces at the knee (62% BW), and 8380 N from the muscles (40% BW; Figure 6, Table 2). Several active muscles insert on the diaphysis (*gastrocnemius*, *vasti lateralis* and *medialis*), which is more robust in heavy rhinos like *C. simum* than in others, helping to sustain more intense joint reaction forces and muscular forces (Mallet et al., 2019). The *gluteus medialis* (GMD) inserts on the greater trochanter are also more robust in heavy rhinos. The lesser trochanter and third trochanter are also more developed in heavy rhinos, but they were not subject to large forces in our model. The lesser trochanter is the insertion of the protractor muscles of the limb, which are expected to be mostly active during locomotion; the third trochanter is the insertion of the *gluteus superficialis*, mainly used in limb abduction (Barone, 2010; Etienne et al., 2021). The *gluteus superficialis* is probably used more during locomotion as well, but the development of the third trochanter might also not indicate the need to resist greater forces, but instead provide a longer moment arm for the muscle, without it exerting necessarily a higher force. Because of the simplifying assumption in our model involving an immobile patellofemoral articulation, here we do not report the force exerted by the patella on the femoral trochlea, which would be linked to the contraction of all heads of the *quadriceps femoris* (*vastus medialis*, *vastus lateralis* and *rectus femoris*). Unlike in the humerus, the joint reaction forces were mostly aligned with the long axis of the femur, due to its more vertical direction, although the forces at the knee had a slightly more craniocaudal direction than the long axis.

4.2.4 | Tibia and fibula

The joint reaction forces exerted at the ankle are likely borne by the tibia alone, or almost so. The fibular contact with the talus is almost parallel to the contact force (Figure 6), and the fibula shows no shape variation with body mass in rhinoceroses (Mallet et al., 2019, 2022). Its role is probably to stabilise the ankle; it may still receive joint reaction forces when the talus is moving mediolaterally.

The tibia was subjected to 32,569 N (154% BW) in our simulation, including 13,038 N from joint reaction forces at the knee (62% BW), 11,195 N at the ankle (53% BW), and 8336 N from muscles (39% BW; Figure 6, Table 2). Several of the most active muscles (e.g. *gluteobiceps*, *quadriceps femoris*) insert proximally on the tibia; this is consistent with the general enlargement of the proximal epiphysis and tibial crest observed in heavier rhinos (Mallet et al., 2019, 2022), compared to the other regions of the tibia which were not subjected to such intense tensile forces. The joint reaction forces were almost perfectly aligned with the long axis of the bone, loading it in compression.

The main force acting on the fibula, despite potential joint reaction forces at the talar and tibial articular surfaces, was a fraction of the force exerted by the *flexor digitorum profundus*. A small force from the *extensor digitorum lateralis* was also possible (up to 435 N). All of those forces were small, which might explain why the fibula's morphological variations appear quite variable and not particularly linked to body mass (Mallet et al., 2019, 2022).

Overall, a relatively straightforward loading pattern is observed in the zeugopod bones (radius, ulna, tibia, fibula), compared with the many different muscular forces observed in the bones of the stylopodium (humerus and femur), which pull in various directions.

This might explain why Mallet et al. (2019) found that the morphology of zeugopodial bones was more affected by body mass and that that of the stylopodial bones was more affected by phylogenetic heritage. Indeed, stylopodial bone shape is likely highly constrained by the various muscular insertions (and thus heterogeneous forces incurred), themselves constrained by the strong phylogenetic heritage apparent for the musculature (Etienne et al., 2021). Zeugopodial bones have muscles that usually pull in more homogeneous directions (Figures 5 and 6), incurring more homogeneous functions, perhaps allowing the bones' shapes to vary more freely with an increasing body mass.

5 | CONCLUSION

As expected, our simulations suggested that antigravity limb muscles are likely to be the most active ones during standing. They generated a moment opposite to that of body weight/ground reaction forces around the joints in order to keep them extended and the rhino limb in a standing position. Muscles with the longest moment arms were indeed favoured because they could generate greater moments for the same force output. The patterns of loading on the different bones were highly variable, illustrating their functional differences. The humerus was subjected to the greatest total force magnitude, coming from a great variety of directions due to the different muscles involved in body weight support and stabilisation inserted into that bone. It exhibits morphofunctional adaptations to further favour the moment-generating capacity of some muscles by increasing their moment arms, such as the development of the intermediate tubercle (*biceps brachii*) and lateral epicondyle (*ulnaris lateralis*). The radius and ulna displayed straightforward patterns. The radius was primarily subjected to high-magnitude joint reaction forces at its extremities, aligned with its long axis. The ulna, however, was subjected to relatively low joint reaction forces, but higher tensile muscular forces than the radius at the proximal extremity of the olecranon (notably from the *triceps brachii*), probably spreading to the entire caudal border of the bone. The femur was similar to the humerus in terms of loading pattern, but the joint reaction forces that the femur was subjected to were more aligned with its long axis than in the humerus. The tibia was subjected to intense compressive joint reaction forces in its caudal half and to intense tension from the various muscles inserted near the tibial crest in its cranial half. The fibula might be subjected to joint reaction forces from the talus and tibia, and to some muscular tension, but still experienced, by far, the lowest forces of all of the long bones. Overall, these data allow more precise inferences about the links between form and function in rhino bones, and could notably be very interesting for microanatomical studies, as bone microanatomy is known to show plastic adaptations to specific forces applied on the bones (e.g. Currey, 2002; Kivell, 2016). Further simulation of locomotion at various gaits (notably galloping) could give more information about the most intense loading conditions experienced by rhino bones, expanding our understanding beyond standing, the most common condition, which we have studied here. Any of these simulations would benefit from more empirical data, especially from in vivo kinematics and kinetics, and ex vivo cadaveric data on tissue properties.

AUTHOR CONTRIBUTIONS

All authors contributed to the study conception, data analysis and interpretation and critical revision of the manuscript and approval of the article. CE additionally developed the musculoskeletal models under the guidance of JRH and drafted the manuscript.

ACKNOWLEDGMENTS

We thank Jamie Maclaren (University of Antwerp) for digitising a white rhino pelvis for the hindlimb model. We thank Ashleigh Wiseman (University of Cambridge) for their advice on modelling and simulation. We also thank Pauline Hanot (UMR 7179, Muséum national d'Histoire naturelle/Centre national de la Recherche Scientifique) for providing horse phalanges to compare with rhinos' for the estimation of joint mobility, and for constructive discussion on that matter. We thank Peter Aerts (University of Antwerp), John A. Nyakatura (Humboldt University of Berlin) and Williams I. Sellers (University of Manchester) for constructive discussions and comments on an early version of the manuscript. We also thank Stephan Milz and Edward Fenton for their editorial work and two anonymous reviewers for their very helpful comments. CE was funded by a doctoral scholarship granted by the Learning Planet Institute and Université Paris-Cité. AH was funded by a European Research Council grant (GRAVIBONE project, ERC-2016-STG-715300).

DATA AVAILABILITY STATEMENT

Muscular data used for the modelling are included in Etienne et al. (2021). The OpenSim models are provided in the Data S2. Bone scans are available in the following MorphoSource project: https://www.morphosource.org/projects/000586533?locale=en.

ORCID

Cyril Etienne https://orcid.org/0000-0002-4548-2934
Alexandra Houssaye https://orcid.org/0000-0001-8789-5545
John R. Hutchinson https://orcid.org/0000-0002-6767-7038

REFERENCES

Alexander, R.M. & Pond, C. (1992) Locomotion and bone strength of the white rhinoceros, *Ceratotherium simum*. *Journal of Zoology*, 227, 63–69. Available from: https://doi.org/10.1111/j.1469-7998.1992.tb04344.x

Alexander, R.M.N., Maloiy, G.M.O., Hunter, B., Jayes, A.S. & Nturibi, J. (1979) Mechanical stresses in fast locomotion of buffalo (*Syncerus caffer*) and elephant (*Loxodonta africana*). *Journal of Zoology*, 189, 135–144. Available from: https://doi.org/10.1111/j.1469-7998.1979.tb03956.x

Anderson, F.C. & Pandy, M.G. (2001) Static and dynamic optimization solutions for gait are practically equivalent. *Journal of Biomechanics*, 34, 153–161. Available from: https://doi.org/10.1016/s0021-9290(00)00155-x

Anderson, L., Brassey, C., Pond, S., Bates, K. & Sellers, W.I. (2023) Investigating the quadrupedal abilities of *Scutellosaurus lawleri* and its implications for locomotor behavior evolution among dinosaurs. *The Anatomical Record*, 306, 2514–2536. Available from: https://doi.org/10.1002/ar.25189

Arnold, E.M., Ward, S.R., Lieber, R.L. & Delp, S.L. (2010) A model of the lower limb for analysis of human movement. *Annals of Biomedical Engineering*, 38, 269–279. Available from: https://doi.org/10.1007/s10439-009-9852-5

Bader, C., Böhmer, C., Abou, M. & Houssaye, A. (2022) How does bone microanatomy and musculature covary? An investigation in the forelimb of two species of martens (*Martes foina*, *Martes martes*). *Journal of Anatomy*, 241, 145–167. Available from: https://doi.org/10.1111/joa.13645

Barone, R. (1999) *Anatomie comparée des mammifères domestiques. Tome 1: ostéologie, 5ème édition*. Paris: Vigot Frères.

Barone, R. (2010) *Anatomie comparée des mammifères domestiques. Tome 2: arthrologie et myologie, 4ème édition*. Paris: Vigot Frères.

Basu, C., Wilson, A.M. & Hutchinson, J.R. (2019) The locomotor kinematics and ground reaction forces of walking giraffes. *Journal of Experimental Biology*, 222, jeb159277. Available from: https://doi.org/10.1242/jeb.159277

Bates, K.T., Manning, P.L., Margetts, L. & Sellers, W.I. (2010) Sensitivity analysis in evolutionary robotic simulations of bipedal dinosaur running. *Journal of Vertebrate Paleontology*, 30, 458–466. Available from: https://doi.org/10.1080/02724630903409329

Becker, J., Mermoz, E. & Linares, J.-M. (2020) Determination of biological joint reaction forces from *in-vivo* experiments using a hybrid combination of biomechanical and mechanical engineering software. *Mechanics & Industry*, 21, 623. Available from: https://doi.org/10.1051/meca/2020088

Bertram, J.E.A. & Biewener, A.A. (1992) Allometry and curvature in the long bones of quadrupedal mammals. *Journal of Zoology*, 226, 455–467. Available from: https://doi.org/10.1111/j.1469-7998.1992.tb07492.x

Biewener, A. (1989) Scaling body support in mammals: limb posture and muscle mechanics. *Science*, 245, 45–48. Available from: https://doi.org/10.1126/science.2740914

Biewener, A. & Patek, S. (2018) *Animal Locomotion*, 2nd edition. New York: Oxford University Press.

Bishop, P.J., Cuff, A.R. & Hutchinson, J.R. (2021) How to build a dinosaur: musculoskeletal modeling and simulation of locomotor biomechanics in extinct animals. *Paleobiology*, 47, 1–38. Available from: https://doi.org/10.1017/pab.2020.46

Bishop, P.J., Falisse, A., de Groote, F. & Hutchinson, J.R. (2021) Predictive simulations of running gait reveal a critical dynamic role for the tail in bipedal dinosaur locomotion. *Science Advances*, 7, eabi7348. Available from: https://doi.org/10.1126/sciadv.abi7348

Bishop, P.J., Michel, K.B., Falisse, A., Cuff, A.R., Allen, V.R., de Groote, F. et al. (2021) Computational modelling of muscle fibre operating ranges in the hindlimb of a small ground bird (*Eudromia elegans*), with implications for modelling locomotion in extinct species. *PLoS Computational Biology*, 17, e1008843. Available from: https://doi.org/10.1371/journal.pcbi.1008843

Bonnan, M.F., Wilhite, D.R., Masters, S.L., Yates, A.M., Gardner, C.K. & Aguiar, A. (2013) What lies beneath: sub-articular long bone shape scaling in eutherian mammals and saurischian dinosaurs suggests different locomotor adaptations for gigantism. *PLoS One*, 8, e75216. Available from: https://doi.org/10.1371/journal.pone.0075216

Cignoni, P., Callieri, M., Corsini, M., Dellepiane, M., Ganovelli, F. & Ranzuglia, G. (2008) MeshLab: an Open-Source Mesh Processing Tool. Proceedings of the 2008 Eurographics Italian Chapter Conference 129–136. https://doi.org/10.2312/LocalChapterEvents/ItalChap/ItalianChapConf2008/129-136

Currey, J.D. (2002) *Bones: structure and mechanics*. Princeton and Oxford: Princeton University Press.

DeMers, M.S., Hicks, J.L. & Delp, S.L. (2017) Preparatory co-activation of the ankle muscles may prevent ankle inversion injuries. *Journal of Biomechanics*, 52, 17–23. Available from: https://doi.org/10.1016/j.jbiomech.2016.11.002

Demuth, O.E., Herbst, E., Polet, D., Wiseman, A.L.A. & Hutchinson, J.R. (2023) Modern three-dimensional digital methods for studying locomotor biomechanics in tetrapods. *Journal of Experimental Biology*, 226, jeb245132. Available from: https://doi.org/10.1242/jeb.245132

Dinerstein, E. (2011) Family Rhinocerotidae (Rhinoceroses). In: Wilson, D.E. & Mittermeier, R.A. (Eds.) *Handbook of the mammals of the world*. Barcelona: Lynx Edicions, pp. 144–181.

Dorn, T.W., Wang, J.M., Hicks, J.L. & Delp, S.L. (2015) Predictive simulation generates human adaptations during loaded and inclined walking. *PLoS One*, 10, e0121407. Available from: https://doi.org/10.1371/journal.pone.0121407

Dudley, R.J., Wood, S.P., Hutchinson, J.R. & Weller, R. (2014) Radiographic protocol and normal anatomy of the hind feet in the white rhinoceros (*Ceratotherium simum*). *Veterinary Radiology & Ultrasound*, 56, 124–132. Available from: https://doi.org/10.1111/vru.12215

Erdemir, A., McLean, S., Herzog, W. & van den Bogert, A.J. (2007) Model-based estimation of muscle forces exerted during movements. *Clinical Biomechanics*, 22, 131–154. Available from: https://doi.org/10.1016/j.clinbiomech.2006.09.005

Etienne, C., Houssaye, A. & Hutchinson, J.R. (2021) Limb myology and muscle architecture of the Indian rhinoceros *Rhinoceros unicornis* and the white rhinoceros *Ceratotherium simum* (Mammalia: Rhinocerotidae). *PeerJ*, 9, e11314. Available from: https://doi.org/10.7717/peerj.11314

Garland, T. (1983) The relation between maximal running speed and body mass in terrestrial mammals. *Journal of Zoology*, 199, 157–170. Available from: https://doi.org/10.1111/j.1469-7998.1983.tb02087.x

Gatesy, S.M., Manafzadeh, A.R., Bishop, P.J., Turner, M.L., Kambic, R.E., Cuff, A.R. et al. (2022) A proposed standard for quantifying 3-D hindlimb joint poses in living and extinct archosaurs. *Journal of Anatomy*, 241, 101–118. Available from: https://doi.org/10.1111/joa.13635

Griffin, T.M., Main, R.P. & Farley, C.T. (2004) Biomechanics of quadrupedal walking: how do four-legged animals achieve inverted pendulum-like movements? *Journal of Experimental Biology*, 207, 3545–3558. Available from: https://doi.org/10.1242/jeb.01177

Harrison, S.M., Whitton, R.C., Kawcak, C.E., Stover, S.M. & Pandy, M.G. (2010) Relationship between muscle forces, joint loading and utilization of elastic strain energy in equine locomotion. *Journal of Experimental Biology*, 213, 3998–4009. Available from: https://doi.org/10.1242/jeb.044545

Harrison, S.M., Whitton, R.C., King, M., Haussler, K.K., Kawcak, C.E., Stover, S.M. et al. (2012) Forelimb muscle activity during equine locomotion. *Journal of Experimental Biology*, 215, 2980–2991. Available from: https://doi.org/10.1242/jeb.065441

Heers, A.M., Rankin, J.W. & Hutchinson, J.R. (2018) Building a bird: musculoskeletal modeling and simulation of wing-assisted incline running during avian ontogeny. *Frontiers in Bioengineering and Biotechnology*, 6, 140. Available from: https://doi.org/10.3389/fbioe.2018.00140

Hermanson, J.W. & MacFadden, B.J. (1992) Evolutionary and functional morphology of the shoulder region and stay-apparatus in fossil and extant horses (Equidae). *Journal of Vertebrate Paleontology*, 12, 377–386. Available from: https://doi.org/10.1080/02724634.1992.10011466

Hermanson, J.W. & Macfadden, B.J. (1996) Evolutionary and functional morphology of the knee in fossil and extant horses (Equidae). *Journal of Vertebrate Paleontology*, 16, 349–357. Available from: https://doi.org/10.1080/02724634.1996.10011321

Hicks, J.L., Uchida, T.K., Seth, A., Rajagopal, A. & Delp, S.L. (2015) Is my model good enough? Best practices for verification and validation of musculoskeletal models and simulations of movement. *Journal of Biomechanical Engineering*, 137, 020905. Available from: https://doi.org/10.1115/1.4029304

Hildebrand, M. (1980) The adaptive significance of tetrapod gait selection. *American Zoologist*, 20, 255–267. Available from: https://doi.org/10.1093/icb/20.1.255

Hildebrand, M. (1989) The quadrupedal gaits of vertebrates: the timing of leg movements relates to balance, body shape, agility, speed, and energy expenditure. *Bioscience*, 39, 766–775. Available from: https://doi.org/10.2307/1311182

Hildebrand, M., Bramble, D.M., Liem, K.F. & Wake, D. (1985) *Functional vertebrate morphology*. Cambridge, USA: Belknap Press of Harvard University Press.

Hodson-Tole, E. (2006) Effects of treadmill inclination and speed on forelimb muscle activity and kinematics in the horse. *Equine and Comparative Exercise Physiology*, 3, 61–72. Available from: https://doi.org/10.1079/ECP200681

Houssaye, A., Waskow, K., Hayashi, S., Cornette, R., Lee, A.H. & Hutchinson, J.R. (2016) Biomechanical evolution of solid bones in large animals: a microanatomical investigation. *Biological Journal of the Linnean Society*, 117, 350–371. Available from: https://doi.org/10.1111/bij.12660

Hutchinson, J.R. (2021) The evolutionary biomechanics of locomotor function in giant land animals. *Journal of Experimental Biology*, 224, jeb217463. Available from: https://doi.org/10.1242/jeb.217463

Hutchinson, J.R., Anderson, F.C., Blemker, S.S. & Delp, S.L. (2005) Analysis of hindlimb muscle moment arms in *Tyrannosaurus rex* using a three-dimensional musculoskeletal computer model: implications for stance, gait, and speed. *Paleobiology*, 31, 676–701. Available from: https://doi.org/10.1666/0094-8373(2005)031[0676:AOHMMA]2.0.CO;2

Kivell, T.L. (2016) A review of trabecular bone functional adaptation: what have we learned from trabecular analyses in extant hominoids and what can we apply to fossils? *Journal of Anatomy*, 228, 569–594. Available from: https://doi.org/10.1111/joa.12446

Lee, H., Kirkland, W.G., Whitmore, R.N., Theis, K.M., Young, H.E., Richardson, A.J. et al. (2014) Comparison of equine articular cartilage thickness in various joints. *Connective Tissue Research*, 55, 339–347. Available from: https://doi.org/10.3109/03008207.2014.949698

Lerner, Z.F., Gadomski, B.C., Ipson, A.K., Haussler, K.K., Puttlitz, C.M. & Browning, R.C. (2015) Modulating tibiofemoral contact force in the sheep hind limb via treadmill walking: predictions from an OpenSim musculoskeletal model. *Journal of Orthopaedic Research*, 33, 1128–1133. Available from: https://doi.org/10.1002/jor.22829

Maclaren, J.A., Hulbert, R.C., Jr., Wallace, S.C. & Nauwelaerts, S. (2018) A morphometric analysis of the forelimb in the genus *Tapirus* (Perissodactyla: Tapiridae) reveals influences of habitat, phylogeny and size through time and across geographical space. *Zoological Journal of the Linnean Society*, 184, 499–515. Available from: https://doi.org/10.1093/zoolinnean/zly019

Macpherson, J.M. (1994) Changes in postural strategy with inter-paw distance. *Journal of Neurology*, 71, 931–940. Available from: https://doi.org/10.1152/jn.1994.71.3.931

Malda, J., de Grauw, J.C., Benders, K.E.M., Kik, M.J.L., van de Lest, C.H.A., Creemers, L.B. et al. (2013) Of mice, men and elephants: the relation between articular cartilage thickness and body mass. *PLoS One*, 8, e57683. Available from: https://doi.org/10.1371/journal.pone.0057683

Mallet, C., Billet, G., Cornette, R. & Alexandra Houssaye, A. (2022) Adaptation to graviportality in Rhinocerotoidea? An investigation through the long bone shape variation in their hindlimb. *Zoological Journal of the Linnean Society*, 196, 1235–1271. Available from: https://doi.org/10.1093/zoolinnean/zlac007

Mallet, C., Billet, G., Houssaye, A. & Cornette, R. (2020) A first glimpse at the influence of body mass in the morphological integration of the limb long bones: an investigation in modern rhinoceroses. *Journal of Anatomy*, 237, 704–726. Available from: https://doi.org/10.1111/joa.13232

Mallet, C., Cornette, R., Billet, G. & Houssaye, A. (2019) Interspecific variation in the limb long bones among modern rhinoceroses—extent and drivers. *PeerJ*, 7, e7647. Available from: https://doi.org/10.7717/peerj.7647

Mallet, C., Houssaye, A., Cornette, R. & Billet, G. (2021) Long bone shape variation in the forelimb of Rhinocerotoidea: relation with size, body mass and body proportions. *Zoological Journal of the Linnean Society*, 196, 1201–1234. Available from: https://doi.org/10.1093/zoolinnean/zlab095

Mancini, I.A.D., Rieppo, L., Pouran, B., Afara, I.O., Braganca, F.M.S., van Rijen, M.H.P. et al. (2019) Effects of body mass on microstructural features of the osteochondral unit: a comparative analysis of 37 mammalian species. *Bone*, 127, 664–673. Available from: https://doi.org/10.1016/j.bone.2019.07.001

Millard, M., Uchida, T., Seth, A. & Delp, S.L. (2013) Flexing computational muscle: modeling and simulation of musculotendon dynamics. *Journal of Biomechanical Engineering*, 135, 0210051–02100511. Available from: https://doi.org/10.1115/1.4023390

Ong, C.F., Hicks, J.L. & Delp, S.L. (2016) Simulation-based design for wearable robotic systems: an optimization framework for enhancing a standing long jump. *IEEE Transactions on Biomedical Engineering*, 63, 894–903. Available from: https://doi.org/10.1109/TBME.2015.2463077

Panagiotopoulou, O., Pataky, T.C. & Hutchinson, J.R. (2019) Foot pressure distribution in white rhinoceroses (*Ceratotherium simum*) during walking. *PeerJ*, 7, e6881. Available from: https://doi.org/10.7717/peerj.6881

Park, S., Lee, S., Yoon, J. & Chae, S.-W. (2019) Finite element analysis of knee and ankle joint during gait based on motion analysis. *Medical Engineering & Physics*, 63, 33–41. Available from: https://doi.org/10.1016/j.medengphy.2018.11.003

Rajagopal, A., Dembia, C.L., DeMers, M.S., Delp, D.D., Hicks, J.L. & Delp, S.L. (2016) Full-body musculoskeletal model for muscle-driven simulation of human gait. *IEEE Transactions on Biomedical Engineering*, 63, 2068–2079. Available from: https://doi.org/10.1109/TBME.2016.2586891

Regnault, S., Hermes, R., Hildebrandt, T., Hutchinson, J.R. & Weller, R. (2013) Osteopathology in the feet of rhinoceroses: lesion type and distribution. *Journal of Zoo and Wildlife Medicine*, 44, 918–927. Available from: https://doi.org/10.1638/2012-0277R1.1

Schaffelhofer, S., Sartori, M., Scherberger, H. & Farina, D. (2015) Musculoskeletal representation of a large repertoire of hand grasping actions in primates. *IEEE Transactions on Neural Systems and Rehabilitation Engineering*, 23, 210–220. Available from: https://doi.org/10.1109/TNSRE.2014.2364776

Schuurman, S.O., Kersten, W. & Weijs, W.A. (2003) The equine hind limb is actively stabilized during standing. *Journal of Anatomy*, 202, 355–362. Available from: https://doi.org/10.1046/j.1469-7580.2003.00166.x

Sellers, W.I. & Manning, P.L. (2007) Estimating dinosaur maximum running speeds using evolutionary robotics. *Proceedings of the Royal Society B*, 274, 2711–2716. Available from: https://doi.org/10.1098/rspb.2007.0846

Seth, A., Hicks, J.L., Uchida, T.K., Habib, A., Dembia, C.L., Dunne, J.J. et al. (2018) OpenSim: simulating musculoskeletal dynamics and neuromuscular control to study human and animal movement. *PLoS Computational Biology*, 14, e1006223. Available from: https://doi.org/10.1371/journal.pcbi.1006223

Shockey, B. (2001) Specialized knee joints in some extinct, endemic, South American herbivores. *Acta Palaeontologica Polonica*, 46, 277–288.

Swanstrom, M.D., Zarucco, L., Hubbard, M., Stover, S.M. & Hawkins, D.A. (2004) Musculoskeletal modeling and dynamic simulation of the thoroughbred equine forelimb during stance phase of the gallop. *Journal of Biomechanical Engineering*, 127, 318–328. Available from: https://doi.org/10.1115/1.1865196 van der Krogt, M.M., Bar-On, L., Kindt, T., Desloovere, K. & Harlaar, J. (2016) Neuro-musculoskeletal simulation of instrumented contracture and spasticity assessment in children with cerebral palsy. *Journal of Neuroengineering and Rehabilitation*, 13, 64. Available from: https://doi.org/10.1186/s12984-016-0170-5

Watson, J. & Wilson, A. (2007) Muscle architecture of *biceps brachii*, *triceps brachii* and *supraspinatus* in the horse. *Journal of Anatomy*, 210, 32–40. Available from: https://doi.org/10.1111/j.1469-7580.2006.00669.x

Willson, A.M., Richburg, C.A., Czerniecki, J., Steele, K.M. & Aubin, P.M. (2020) Design and development of a quasi-passive transtibial biarticular prosthesis to replicate gastrocnemius function in walking. *Journal of Medical Devices*, 14, 0250011–0250016. Available from: https://doi.org/10.1115/1.4045879

Witte, T.H., Knill, K. & Wilson, A.M. (2004) Determination of peak vertical ground reaction force from duty factor in the horse (*Equus caballus*). *Journal of Experimental Biology*, 207, 3639–3648. Available from: https://doi.org/10.1242/jeb.01182

Zajac, F.E. (1989) Muscle and tendon: properties, models, scaling, and application to biomechanics and motor control. *Critical Reviews in Biomedical Engineering*, 17, 359–411.

SUPPORTING INFORMATION

Additional supporting information can be found online in the Supporting Information section at the end of this article.

How to cite this article: Etienne, C., Houssaye, A., Fagan, M.J. & Hutchinson, J.R. (2024) Estimation of the forces exerted on the limb long bones of a white rhinoceros (*Ceratotherium simum*) using musculoskeletal modelling and simulation. *Journal of Anatomy*, 00, 1–18. Available from: https://doi.org/10.1111/joa.14041